PHOTONICS Research

Dielectric metasurface evolution from bulk to monolayer by strong coupling of quasi-BICs for second harmonic boosting

Yinong Xie,[1,2,†] Qianting Chen,[1,2,†] Jin Yao,[3] Xueying Liu,[1,2] Zhaogang Dong,[4,5] and Jinfeng Zhu[1,2,*]

[1]Institute of Electromagnetics and Acoustics and Key Laboratory of Electromagnetic Wave Science and Detection Technology, Xiamen University, Xiamen 361005, China
[2]Shenzhen Research Institute of Xiamen University, Shenzhen 518057, China
[3]Department of Electrical Engineering, City University of Hong Kong, Hong Kong 999077, China
[4]Institute of Materials Research and Engineering (IMRE), Agency for Science, Technology and Research (A*STAR), Singapore 138634, Singapore
[5]Department of Materials Science and Engineering, National University of Singapore, Singapore 117575, Singapore
[†]These authors contributed equally to this work.
*Corresponding author: nanoantenna@hotmail.com

Received 27 November 2023; revised 1 February 2024; accepted 4 February 2024; posted 6 February 2024 (Doc. ID 514140); published 1 April 2024

2D materials are promising candidates as nonlinear optical components for on-chip devices due to their ultrathin structure. In general, their nonlinear optical responses are inherently weak due to the short interaction thickness with light. Recently, there has been great interest in using quasi-bound states in the continuum (q-BICs) of dielectric metasurfaces, which are able to achieve remarkable optical near-field enhancement for elevating the second harmonic generation (SHG) emission from 2D materials. However, most studies focus on the design of combining bulk dielectric metasurfaces with unpatterned 2D materials, which suffer considerable radiation loss and limit near-field enhancement by high-quality q-BIC resonances. Here, we investigate the dielectric metasurface evolution from bulk silicon to monolayer molybdenum disulfide (MoS_2), and discover the critical role of meta-atom thickness design on enhancing near-field effects of two q-BIC modes. We further introduce the strong-coupling of the two q-BIC modes by oblique incidence manipulation, and enhance the localized optical field on monolayer MoS_2 dramatically. In the ultraviolet and visible regions, the MoS_2 SHG enhancement factor of our design is 10^5 times higher than that of conventional bulk metasurfaces, leading to an extremely high nonlinear conversion efficiency of 5.8%. Our research will provide an important theoretical guide for the design of high-performance nonlinear devices based on 2D materials.

https://doi.org/10.1364/PRJ.514140

1. INTRODUCTION

As a widely observed nonlinear effect of optics, second harmonic generation (SHG) has been extensively applied in spectroscopy, sensing, and image processing [1–4]. Conventionally, there are several bulk materials used to build the optical devices of SHG, such as lithium niobate ($LiNbO_3$) and gallium arsenide (GaAs) [5–7]. In the past few years, 2D materials are found as promising multilayer or monolayer materials for constructing on-chip SHG devices, since they have the considerable nonlinear susceptibility $\chi^{(2)}$ in an ultrathin thickness (from several angstroms to several nanometers) [8–10]. Typically, such a small thickness makes the weak interaction between 2D materials with the incident light, and thus it requires the light trapping structure to enhance the localized optical near field significantly [11]. In view of this motivation, researchers have investigated the use of various plasmonic or dielectric metasurfaces for elevating the SHG responses of 2D materials [12–15]. Compared with the plasmonic counterparts, dielectric metasurfaces are much more attractive for efficient enhancement of nonlinear interaction in 2D materials, because they have much lower intrinsic optical losses governed by radiation leakage only [16–18] and provide higher quality factor (Q-factor) responses [18–20]. Particularly, by introducing the symmetry breaking, dielectric metasurfaces can exhibit the quasi-bound states in the continuum (q-BICs) [21,22] and have the potential to accomplish an extremely high Q-factor for the dramatical enhancement on SHG of 2D materials. So far, employing q-BICs of dielectric metasurfaces has been becoming the research hotspot on nonlinear optics of 2D materials [23,24]. However, most existing studies focus on designing the q-BIC dielectric metasurfaces with asymmetric nanostructure units of bulk materials, and combine them with 2D materials

to enhance the SHG effect [23,25]. Such bulk metastructure design has a thickness with a giant difference from that of 2D materials. Its larger thickness exhibits distinct out-of-plane asymmetry, which induces considerable optical dissipation of radiation [26,27]. This not only suppresses the high Q-factor resonance performance of the metasurface, but also hinders efficient light field concentration on 2D materials. Very recently, researchers have found that one can dramatically lower the optical dissipation by reducing the patterned layer thickness of a dielectric metasurface from the bulk to the sheet [28,29], which might be promising for enhancing the SHG of 2D materials. Despite this, there is a critical limitation on ultrathin nanopattern fabrication of bulk metastructures [30]. Therefore, it is still essential to pursue a feasible mechanism based on the q-BIC dielectric metasurface for boosting the SHG of 2D materials.

Herein, we propose the design of a dielectric q-BIC metasurface based on the evolution from bulk material to monolayer material. We adopt the meta-atom unit of monolayer molybdenum disulfide (MoS_2) under a specific geometrical asymmetry, which supports two q-BIC modes with much higher Q-factors than the traditional bulk silicon (Si) metasurface design. By tuning the incident angle of the incident light, we obtain a resonance response with the extremely high Q-factor. It is attributed to the strong coupling of two q-BIC modes. The intensive near-field enhancement supported by such a strong coupling mechanism boosts the SHG of monolayer MoS_2. Our study will provide a theoretical guide for the development of high-performance nonlinear photonic devices based on 2D materials.

2. DESIGN AND METHODS

The evolution from bulk to monolayer metasurfaces is shown in Fig. 1. There are three geometric manipulation mechanisms, namely, symmetrical breaking, thickness transformation, and angle control. The in-plane asymmetry configuration of a metasurface enables two q-BIC modes. Based on such asymmetry, we implement the transformation from bulk Si to sheet Si and monolayer MoS_2. In our design, the monolayer MoS_2 is adopted as a nonlinear optical material, which has a large nonlinear susceptibility tensor $\chi^{(2)}$ of ~150 pm/V in the visible and near-infrared regions [31]. The meta-atoms of these metasurfaces are asymmetric rectangular pairs of bulk Si, sheet Si, and monolayer MoS_2, respectively. They also consist of a silicon nitride (Si_3N_4) waveguide layer with a thickness of $t = 200$ nm and the silicon dioxide (SiO_2) substrate. For the asymmetric pair of monolayer MoS_2 metasurfaces, we provide a feasible nanofabrication process (see details in Appendix A). The periods of metasurfaces along the x- and y-directions are p and $p/2$, respectively, where $p = 560$ nm. The rectangular lengths in the x-direction for each asymmetry pair are l ($l = w = p/4$, where w represents the y-direction rectangular width) and $l + \Delta l$, respectively, while the asymmetry parameter is defined as $\alpha = \Delta l/l$. The thicknesses of the bulk Si, sheet Si, and MoS_2 are denoted as d_1, d_2, and d_3, respectively. According to the literature, the refractive indexes of Si_3N_4 and SiO_2 are assumed as 2.02 and 1.45, respectively [32]. The complex refractive index parameters of Si, bulk, and monolayer MoS_2

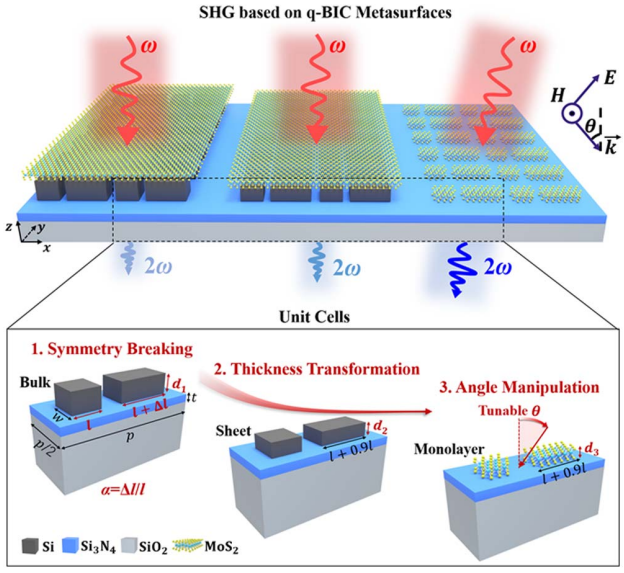

Fig. 1. Schematic diagram for the evolution from bulk to monolayer q-BIC metasurfaces, where the symbols p, t, w, d_1, d_2, d_3, and θ denote the period, thickness of waveguide layer, width and heights of various asymmetrical rectangular pairs, and the incident angle, respectively.

are based on the experimental data [33,34] (see details in Appendix B). Particularly, the monolayer MoS_2 has a high refractive index with the infinitesimal extinction coefficient in this spectral range [35].

With the aim of studying the optical responses of metasurfaces, we employ the simulation modules for nonlinear optics by the commercial software COMSOL Multiphysics, which is based on the finite element method. In the simulation, Floquet boundary conditions are adopted on the unit cells of metasurfaces in x- and y-directions. The wave ports are used at the top and bottom of z-direction. The optical incidence is applied from the top side of each meta-atom with the incident angle of θ and the intensity of 0.001 GW/cm^2. A full-wave simulation is conducted for the linear optical process, in which the localized near-field distributions of the fundamental wavelength are recorded and used to determine the nonlinear polarization as below [36]:

$$\vec{P}^{(2)}(2\omega) = \varepsilon_0 \chi^{(2)} \vec{E}^2(\omega), \tag{1}$$

where the angular frequency is $\omega = 2\pi/\lambda_r$, λ_r is the resonance wavelength, ε_0 is the vacuum permittivity, and $\vec{E}(\omega)$ denotes the localized electric field inside the nonlinear material at the fundamental wavelength. The nonlinear polarization is used as the excitation source for the SHG process. The SHG conversion efficiency is determined by the ratio $P_{2\omega}/P_{\omega}$ [37], where $P_{2\omega}$ and P_{ω} represent the SHG signal power and pumping power of the fundamental wavelength, respectively.

3. RESULTS AND DISCUSSION

A. High-Q Metasurfaces Empowered by In-Plane Asymmetry q-BIC and Thickness Evolution

We first investigate the optical properties of bulk Si metasurfaces with in-plane symmetry breaking. Their transmittance

spectra demonstrate two resonances marked as q-BIC$_1$ and q-BIC$_2$, respectively, as observed in Fig. 2(a). When α changes from 1 to 0.05, the two resonances have the blue shift with a reduced full width at half maximum (FWHM), which indicates the variation tendency towards an extremely high Q-factor ($Q = \lambda_r/\mathrm{FWHM}$, where λ_r denotes the resonance wavelength). As α equals zero, the FWHMs of two resonances disappear, indicating two symmetry-protected BICs [38]. Here, the Q-factors of the two q-BIC modes can be fitted with $Q \propto \alpha^{-2}$ (see details in Appendix C). Such property is also observed in some previous studies [18,27]. In the resonance system of an all-dielectric metasurface, a high-Q response implies the good capability to support high optical field enhancement [25], which is quite beneficial to strengthen the effects of nonlinear materials. In addition, the Q-factor is determined by the total rate of optical loss γ ($Q = \omega/2\gamma$) in a q-BIC system, where $\gamma = \gamma_{\mathrm{rad}} + \gamma_{\mathrm{par}}$, γ_{rad} is the radiative loss, and γ_{par} represents the parasitic loss. Ideally, the dielectric metasurfaces are assumed to have negligible parasitic loss ($\gamma_{\mathrm{par}} \approx 0$) [39], while the radiative loss γ_{rad} increases quadratically with the asymmetry parameter, namely, $\gamma_{\mathrm{rad}} \propto \alpha^2$ [23]. Therefore, one can dramatically raise the Q-factor by decreasing the asymmetry factor α at the state of q-BIC [39,40].

Since achieving the high-Q response is crucial for enhancing nonlinear effects, we continue to pursue another way to elevate the Q-factor of metasurfaces. As shown in Fig. 2(b), we fix the in-plane asymmetry of $\alpha = 0.9$ for the two above-mentioned q-BIC modes, and study the influence of asymmetry pair thickness d_2 on the Q-factor. It is observed that the Q-factors of both q-BIC resonances for $d_2 = 10$ nm are much larger than those for $d_2 = 100$ nm. In fact, the Q-factors of the two q-BIC modes can be described as the two functions of d_2, respectively (see details in Appendix C). They demonstrate the relationship of $Q \propto d_2^{-2}$ between the Q-factor and asymmetry pair thickness. This is similar to the correlation between the Q-factor and asymmetry factor. It is because the reduction of asymmetry pair thickness lowers the radiative loss. The asymmetry pair thickness can be used as a tuning factor like α to manipulate the radiative loss of q-BIC[29], that is, $\gamma_{\mathrm{rad}} \propto d_2^2$. For the thick asymmetry pair with large d_2, the Q-factor of q-BIC is limited by higher radiative losses γ_{rad} due to distinct out-of-plane asymmetry. By thinning d_2 from 100 nm to 10 nm, the volumes of each asymmetry pair progressively decrease. Such reduction will suppress the radiation channel propagating outside the system, leading to a substantial decrease in radiative loss. As a result, when $d_2 = 10$ nm ($\alpha = 0.9$), the Q-factors can reach up to 13,751 and 14,254, which are higher than those obtained when $\alpha = 0.1$ ($d_1 = 100$ nm) (see details in Appendix D). This result proves that the asymmetry pair thickness evolution can be also used as a vital factor to increase the Q-factor of q-BIC in addition to tuning the in-plane asymmetry factor.

Although the use of traditional Si is readily available, the fabrication of its 2D counterpart still faces great challenges [30]. As a natural 2D material, MoS_2 can be easily accessed to the monolayer thickness. Therefore, we next focus on using MoS_2 as the material of asymmetry pairs instead of Si. The simulated transmittance spectra for various MoS_2 thicknesses in Fig. 2(c) also show two resonance modes. When d_3 is changed from 50 nm to 0.65 nm at the fixed α value of 0.9, the two q-BIC modes also show the trend of blue shift with

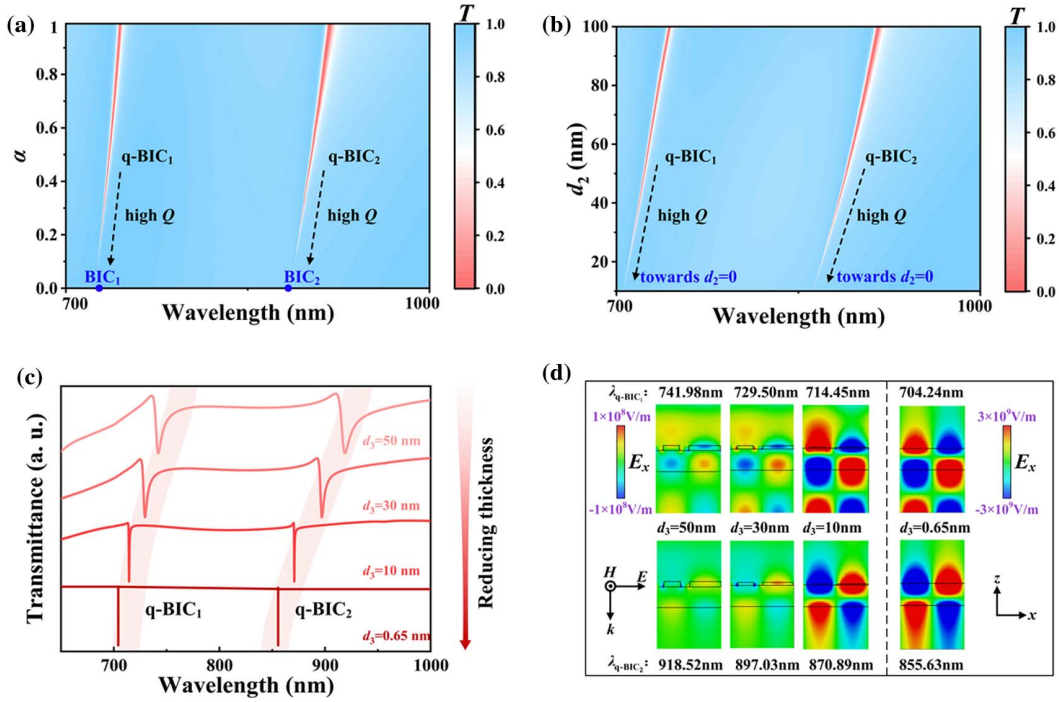

Fig. 2. (a) Transmittance of Si metasurface with in-plane asymmetric q-BIC as a function of α, where $d_1 = 100$ nm. (b) Transmittance of Si metasurface with in-plane asymmetric q-BIC as a function of d_2, where $\alpha = 0.9$. (c) Transmittance of metasurface as a function of MoS_2 thickness d_3, where $\alpha = 0.9$. (d) Electric field distributions of metasurfaces for different MoS_2 thicknesses at the resonance wavelengths of q-BIC$_1$. For all the figures, $p = 560$ nm.

dramatically increased Q-factors. This is due to the reduction of effective refractive index induced by thinning asymmetry pairs. For the metasurface of the MoS_2 monolayer (0.65 nm), the Q-factors of q-BIC_1 and q-BIC_2 can be up to 1.0×10^6 and 1.4×10^6, respectively (see details in Appendix D).

The q-BICs with ultrahigh Q-factors are usually associated with the significant enhancement of the localized electric field surrounding the metasurface [41]. Such field enhancement should be beneficial to strengthen the nonlinear polarization, according to Eq. (1). In view of this, we plot the electric field distributions in Fig. 2(d) for metasurfaces with different MoS_2 thicknesses at the resonance wavelengths of q-BIC_1 and q-BIC_2, respectively. The electric field distributions at q-BIC_2 indicate a typical feature of guided mode resonance (GMR), which are induced by the leaky guided mode [42]. At the resonance wavelength of q-BIC_1, the presence of multiple interference modes in the waveguide layer indicates that it is the higher-order GMR mode [43]. Notably, decreasing the thickness of MoS_2 boosts the field confinement around the asymmetry pair of MoS_2, as shown in Fig. 2(d). The electric field intensity for the monolayer MoS_2 is two orders greater than that of the 50 nm thickness. This significant enhancement of the localized near field indicates the much stronger light-matter interaction per unit area in the monolayer MoS_2, which is critical to elevate the efficiency of energy utilization by nonlinear effects of MoS_2.

We continue to investigate the influence of α on the BIC-based Q-factors of monolayer metasurfaces in Figs. 3(a) and 3(b). Like the conventional Si counterpart, they have an increase of Q-factors with the decrease of α for both q-BIC_1 and q-BIC_2 modes. The resonance dips of both q-BIC modes vanish when α equals zero, suggesting the states of non-radiative BIC. We further calculate the Q-factors of the two resonance modes in Figs. 3(c) and 3(d), which can be also fitted with $Q \propto \alpha^{-2}$ and demonstrate the physical features of q-BIC modes. Specifically, the Q-factors of the two q-BIC modes can both reach an ultrahigh level of 10^7 for $\alpha = 0.1$. Therefore, the tuning of the asymmetry factor could further elevate the Q-factors of q-BIC resonances based on monolayer MoS_2 metasurfaces, which would be promising to enhance the localized electric field like the thickness engineering of MoS_2 metasurfaces exhibited in Fig. 2(d).

B. Metasurface of Monolayer MoS_2 Empowered by Strong Coupling of q-BICs

In the above discussion, the two high-Q resonances of q-BIC modes are achieved through the thickness evolution from bulk to monolayer metasurfaces and the tuning of the asymmetric factor. These two high-Q modes stem from the high-order and low-order GMR modes, respectively. Previous research has illuminated that neighboring GMR modes could have electromagnetic coupling under oblique incidence, which leads to a higher Q-factor of resonance [42]. Thus, we next investigate the coupling of the two q-BIC modes under oblique incidence in order to further boost the Q-factor for a higher localized electric field. As shown in Fig. 4(a), when the incident angle changes from 4° to 8°, the resonance wavelengths of q-BIC_1 and q-BIC_2 move towards the directions of long and short wavelengths, respectively, and get close to each other. In particular, when the incident angle increases to 10.5°, there is only

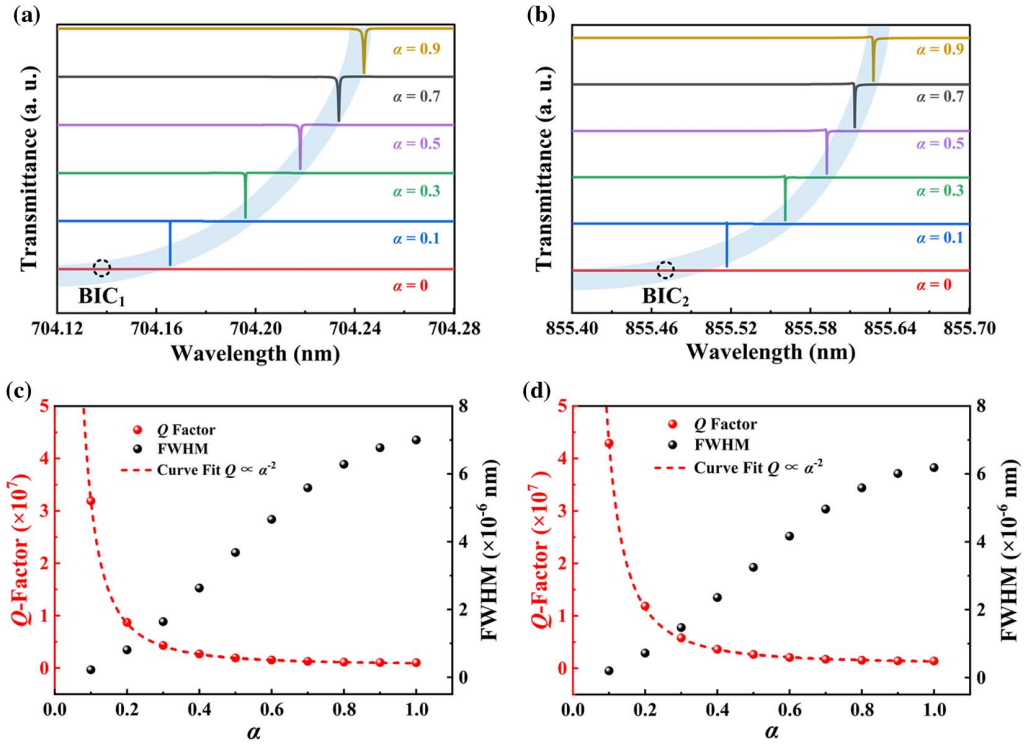

Fig. 3. (a), (b) Transmittance spectra of monolayer MoS_2 metasurface as α changes from 0 to 0.9 for (a) q-BIC_1 and (b) q-BIC_2. (c), (d) Q-factor and FWHM as functions of α for (c) q-BIC_1 and (d) q-BIC_2.

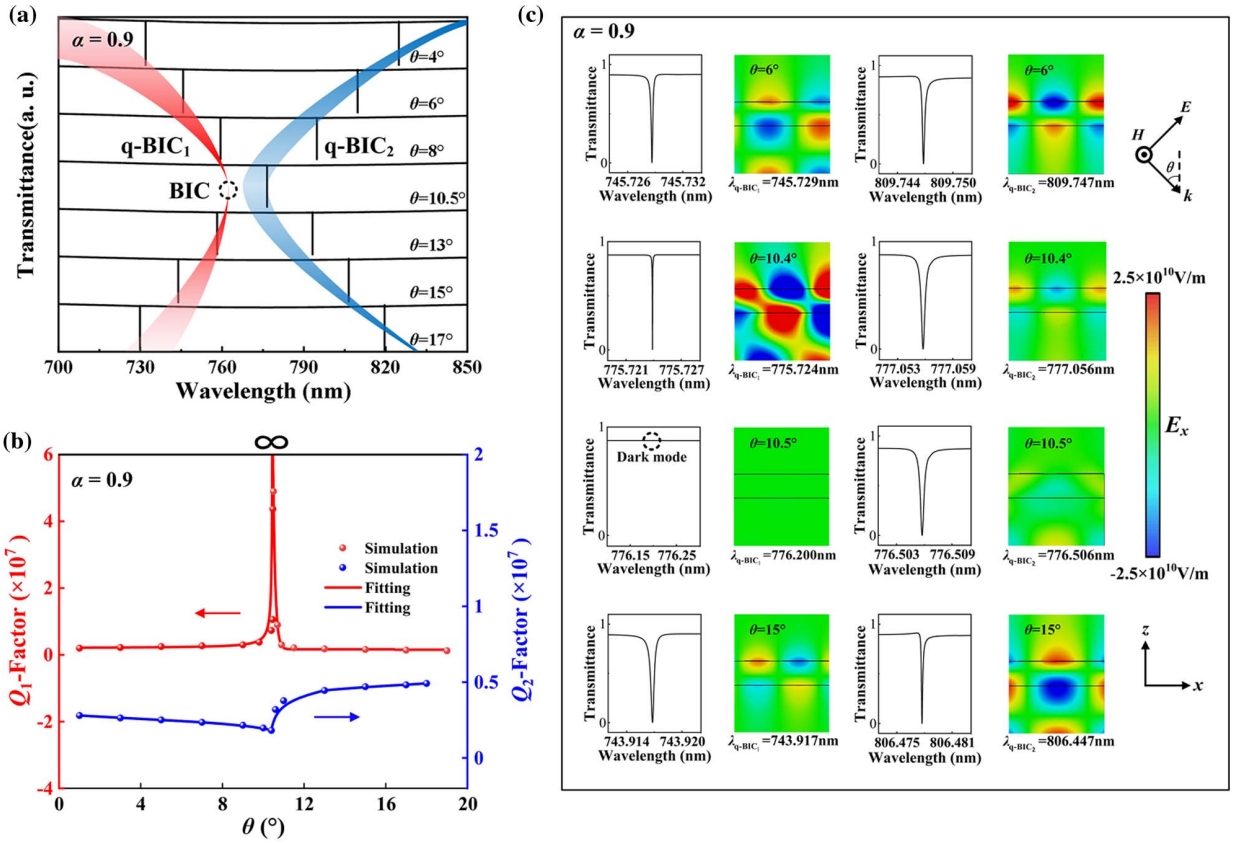

Fig. 4. (a) Resonance behavior of q-BIC$_1$ and q-BIC$_2$ as incident angle θ changes from 4° to 17°. (b) Q-factors of q-BIC$_1$ and q-BIC$_2$ with the change of θ. (c) Transmittance spectra and the corresponding electric field distributions for four incident angles of 6°, 10.4°, 10.5°, and 15°, respectively.

one resonance feature observed on the spectrum around the wavelength of 776.505 nm. This is because the radiation feature of q-BIC$_1$ mode disappears and is transformed into the distinct feature of Friedrich-Wintgen BIC mode [44]. As the incident angle goes over 10.5° and increases from 13° to 17°, the two resonance features of q-BIC$_1$ and q-BIC$_2$ modes can be re-observed, and they continue to move towards the directions of long and short wavelengths. The angle-resolved transmittance spectra show an anti-crossing behavior denoted by the red and blue bands, which implies the strong coupling of the two q-BIC modes and can be described by the following equation [45]:

$$\begin{bmatrix} E_{\mathrm{BIC}_1} + i\gamma_{\mathrm{BIC}_1} & g \\ g & E_{\mathrm{BIC}_2} + i\gamma_{\mathrm{BIC}_2} \end{bmatrix} \begin{pmatrix} \alpha \\ \beta \end{pmatrix} = E_{1,2} \begin{pmatrix} \alpha \\ \beta \end{pmatrix}, \quad (2)$$

where $E_{\mathrm{BIC1,2}}$ and $\gamma_{\mathrm{BIC1,2}}$ denote the energy and damping rate for the uncoupled q-BIC$_1$ and q-BIC$_2$, respectively. g is the coupling strength between the two coupled modes. α and β are used to describe the proportions of two coupled q-BIC modes, and $E_{1,2}$ denotes the energy of two coupled q-BIC modes, respectively, which can be expressed as follows:

$$E_{1,2} = \frac{1}{2}[E_{\mathrm{BIC}_1} + E_{\mathrm{BIC}_2} + i(\gamma_{\mathrm{BIC}_1} + \gamma_{\mathrm{BIC}_2})] \pm \sqrt{g^2 + \frac{[E_{\mathrm{BIC}_1} - E_{\mathrm{BIC}_2} + i(\gamma_{\mathrm{BIC}_1} - \gamma_{\mathrm{BIC}_2})]^2}{4}}, \quad (3)$$

where $E_{\mathrm{BIC1}} - E_{\mathrm{BIC2}} = 0$ represents the energy of two q-BIC modes at the anti-crossing point, and we can obtain the following expression:

$$E_{1,2} = \frac{1}{2}[E_{\mathrm{BIC}_1} + E_{\mathrm{BIC}_2} + i(\gamma_{\mathrm{BIC}_1} + \gamma_{\mathrm{BIC}_2})] \pm \sqrt{g^2 - \frac{(\gamma_{\mathrm{BIC}_1} - \gamma_{\mathrm{BIC}_2})^2}{4}}. \quad (4)$$

Based on Eq. (4), we can have the energy of Rabi splitting as below:

$$2\hbar\Omega = 2\sqrt{g^2 - \frac{(\gamma_{\mathrm{BIC}_1} - \gamma_{\mathrm{BIC}_2})^2}{4}}. \quad (5)$$

When the strong coupling of two q-BIC modes occurs, the following criteria should be satisfied [46,47]:

$$\begin{cases} g > \frac{|\gamma_{\mathrm{BIC}_1} - \gamma_{\mathrm{BIC}_2}|}{2}, \\ g > \sqrt{\frac{\gamma_{\mathrm{BIC}_1}^2 + \gamma_{\mathrm{BIC}_2}^2}{2}}. \end{cases} \tag{6}$$

In this case, we have $\theta = 10.5°$, $\frac{|\gamma_{\mathrm{BIC}_1} - \gamma_{\mathrm{BIC}_2}|}{2} = 3.4 \times 10^{-4}$ meV, $\sqrt{\frac{\gamma_{\mathrm{BIC}_1}^2 + \gamma_{\mathrm{BIC}_2}^2}{2}} = 1.42 \times 10^{-3}$ meV, and $g = 0.14$ meV, which proves that it is a state of strong coupling.

We conduct a further evaluation of the Q-factor evolution of two q-BIC modes under oblique incidence, as illustrated in Fig. 4(b). As the incident angle increases from 0° to 10.5°, the Q-factor of q-BIC_1 exhibits a sharp increase towards infinity, while that of q-BIC_2 decreases gradually, reaching its minimum at 10.5°. To reveal the physics, we present an enlarged view of the transmittance spectra for various incident angles and the corresponding localized electric field distributions in Fig. 4(c). At the incident angle of 6°, the electric field distribution clearly exhibits a high-order mode feature at $\lambda_{\text{q-BIC1}}$, whereas the low-order mode is observed at $\lambda_{\text{q-BIC2}}$. When the angle is 10.4°, the two modes are very close to the state of Friedrich-Wintgen BIC and a clear mode hybridization is observed at the wavelength of 775.724 nm. This denotes the feature of strong coupling, leading to energy redistribution through the two modes. Consequently, the q-BIC_1 mode demonstrates the ultranarrow FWHM and ultrahigh electric field intensity, which are promising for the high-performance SHG device. At the incident angle of 10.5°, the destructive interference launches the dark mode, which collapses the radiation channel and prohibits the coupling to external radiation [48,49]. As the angle increases to 15°, the vanished near-field feature re-emerges, and the two modes undergo band flip, wherein their respective electric field distributions interchange. In combination with the tuning of α on the strong coupling condition, we can further enhance the Q-factor to an extremely high level of 10^8 (see details in Appendix D).

C. SHG Enhancement in Monolayer MoS_2 Metasurface

Based on the proposed monolayer MoS_2 metasurface with the ultrahigh Q-factor, we next evaluate its performance for nonlinear optics. We compare the SHG conversion efficiency of the monolayer MoS_2 metasurface to that of the Si metasurface coated by an unpatterned monolayer MoS_2, as shown in Fig. 5. When the metasurface is excited by a pump laser with normal incidence, the SHG conversion efficiencies of monolayer metasurfaces for both q-BIC_1 and q-BIC_2 are about 10^4 times higher than that of the Si metasurface. Particularly, when the incident angle is 10.4°, the two q-BIC modes are strongly coupled and the SHG conversion efficiency is dramatically enhanced, approaching 5.8% at the wavelength of 383.294 nm.

In order to reveal the nonlinear optical effects, we use the enhancement factor (EF) to quantify the increase of SHG intensity on the metasurface in comparison with the natural homogeneous MoS_2 monolayer. The monolayer MoS_2 metasurface with strong coupling q-BIC exhibits a significantly increased EF of 2.8×10^{10}, which is 10^4 times larger than that of the Si metasurface. Such high nonlinear performance is attributed to the electric field enhancement near the monolayer MoS_2, as indicated in inset (I) of Fig. 5, which can be determined as below [50]:

$$\left|\frac{E_{\mathrm{avg}}}{E_{\mathrm{inc}}}\right|^2 = \frac{\iiint |E|^2 \mathrm{d}V}{|E_{\mathrm{inc}}|^2 \, V}, \tag{7}$$

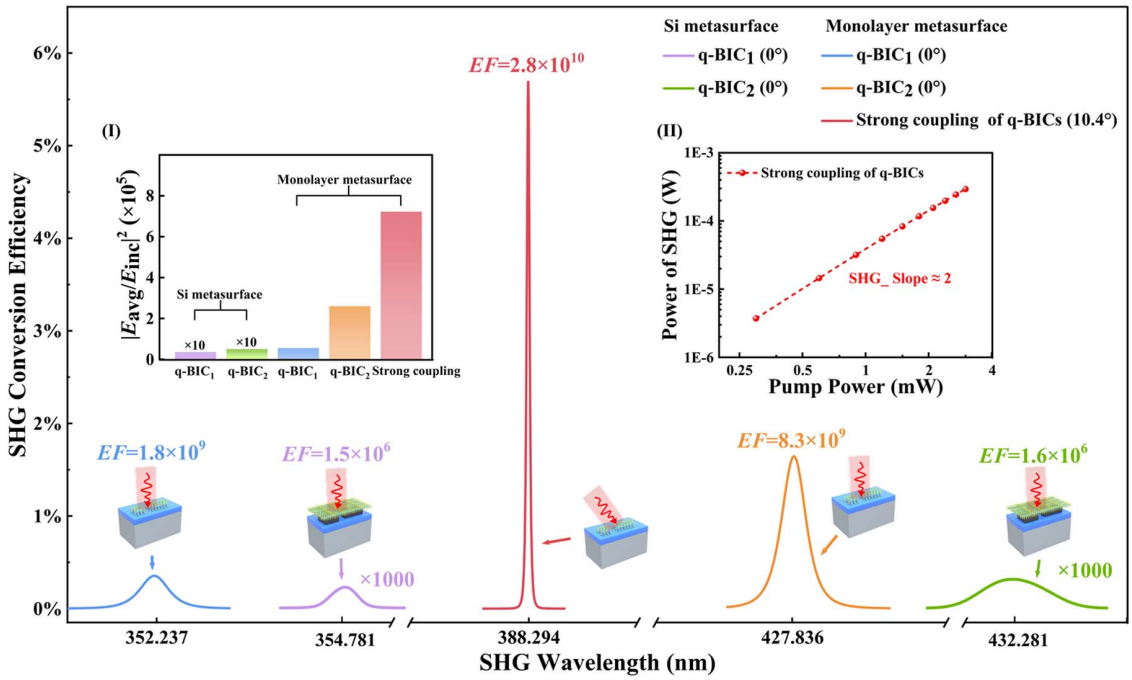

Fig. 5. SHG response and enhancement factor for monolayer MoS_2 metasurface and sheet Si (10 nm thick) metasurface with monolayer MoS_2. Inset (I) denotes the average electric field enhancement factors for various modes. Inset (II) represents the power dependence of SHG in logarithmic scale. Here α is fixed at 0.9.

Table 1. Existing SHG Conversion Efficiency on the Different Structures

No.	I_0 [GW/cm^2]	$\lvert\chi^{(2)}\rvert_{max}$ [pm/V]	SHG Enhancement Factor	SHG Conversion Efficiency [%]	Structures	Refs.
1	0.5	27	—	5×10^{-4}	z-cut $LiNbO_3$ thin film	[51]
2	2.05	25	—	4.2×10^{-4}	$LiNbO_3$ GMR pattern	[52]
3	2.4	68	—	3×10^{-2}	$LiNbO_3$ membrane	[37]
4	~0.001	~200	5×10^3	—	Si with monolayer MoS_2	[53]
5	1	~1700	—	$\sim 10^{-8}$	Bulk MoS_2 nanoresonators	[33]
6	7.2	80	565	—	Two multilayer GaSe on top of SiO_2/Si substrate	[54]
7	**0.001**	**150**	**$> 10^9$**	**5.8**	**Asymmetry pair of monolayer MoS_2**	**This work**

where E, E_{avg}, E_{inc}, and V denote the electric field intensity in the monolayer MoS_2, average value of electric field intensity, incident electric field intensity, and volume of MoS_2, respectively. To further validate the SHG process, we analyze the power as a function of signal intensity, as shown in the double logarithmic plots of inset (II) in Fig. 5. The line shows the fit with a quadratic dependence, which demonstrates the typical feature of SHG.

Finally, we compare the SHG conversion efficiency and EF of the proposed monolayer metasurface with some pioneer studies, as presented in Table 1. Despite lower pump intensities, the EF of our metasurface is 10^5 times larger than that of previous research using a Si metasurface, which implies its good nonlinear performance for future SHG.

4. CONCLUSIONS

In summary, we propose a dielectric metasurface empowered by two high-Q q-BIC modes, which are based on symmetry breaking and thickness transformation on the meta-atom. Particularly, along with the evolution from bulk Si to monolayer MoS_2, the radiation loss of the metasurface is greatly reduced. We further utilize the strong coupling of the two q-BIC resonances by angle manipulation, and achieve an extremely high Q-factor up to 10^8, which also excites the exceptional near-field enhancement on monolayer MoS_2. Our theoretical research elevates the SHG conversion efficiency significantly and will inspire more nonlinear optical studies of 2D materials using q-BICs.

APPENDIX A: FABRICATION PROCESS OF THE MONOLAYER PATTERNED MoS_2 METASURFACE

The fabrication process flow of the symmetrical pair of the monolayer MoS_2 metasurface is shown in Fig. 6. The detailed steps are given below [55].

(1) The prepared bulk MoS_2 is coated with a 100 nm thick layer of gold by thermal evaporation.

(2) The patterned thick resist adapts the standard photolithography technique. The photoresist is spun onto the gold-evaporated surface of bulk MoS_2 flakes using a two-layer process. The resist is baked at 110°C for 3 min following each spin. The resist is exposed with a chrome/glass contact transparency mask for 10 s and subsequently developed for 4 min in deionized water.

(3) Without removing the patterned photoresist layer, the exposed gold is etched in the KI/I_2. This step exposes the MoS_2 that is not to be transferred, while the to-be-transferred material remains masked by the gold and photoresist. The sample is rinsed in deionized water.

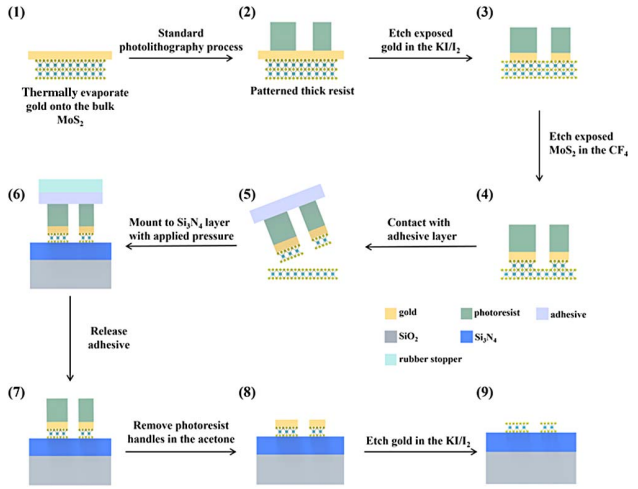

Fig. 6. Fabrication process flow of asymmetry pair of monolayer MoS_2 metasurface.

(4) The patterned flake is then exposed to a 30 s etch in CF_4 plasma to remove at least one atomic layer of the MoS_2 from unmasked regions.

(5) Thermal release tape is brought into contact with the remaining photoresist pattern. Light manual pressure is applied by brushing rubber-tipped tweezers against the back side of the tape, and the tape, loaded now with the pattern, is peeled by hand from the bulk flake.

(6) The SiO_2/Si_3N_4 substrate is treated in O_2 plasma for 5 min. It is then placed on a hot plate at 80°C for at least 5 min. The tape, loaded with the patterned material, is placed onto the heated substrate, and pressure is applied to the tape/substrate stack for 5 min using a weight atop a rubber stopper. The purpose of the rubber is to distribute the load uniformly over the uneven microtopography of the patterned tape's surface.

(7) The SiO_2/Si_3N_4 substrate with the loaded tape is moved to a hot plate at 160°C to trigger the release of the thermal tape.

(8) The transferred stack is now adhered to the SiO_2/Si_3N_4 substrate and is placed in acetone to remove the photoresist.

(9) The remaining gold is stripped in the KI/I_2, and the sample is rinsed in deionized water. Finally, the patterned monolayer MoS_2 metasurface is obtained.

APPENDIX B: OPTICAL PARAMETERS OF Si AND MoS_2

N-type high-purity Si (99.999%) is purchased from Zhongnuo Advanced Material (Beijing) Technology Co., Ltd. and characterized by a spectroscopic ellipsometer (RC2D, J. A. Woollam, United States); the optical parameters of Si are shown in Fig. 7(a). The optical parameters of bulk and monolayer MoS_2 are obtained from Refs. [33,34], as shown in Figs. 7(b) and 7(c).

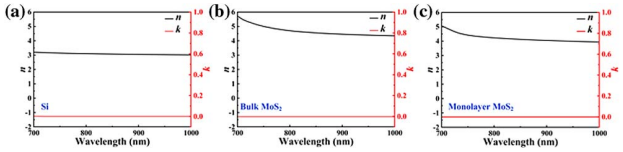

Fig. 7. Real and imaginary parts of the refractive index for (a) Si, (b) bulk MoS_2, and (c) monolayer MoS_2.

APPENDIX C: DEPENDENCE OF THE Q-FACTOR FOR THE TWO Q-BIC MODES ON THE ASYMMETRY PARAMETER α AND THE ASYMMETRY PAIR THICKNESS d_2

The Q-factors of the two q-BIC modes can be fitted with $Q \propto \alpha^{-2}$, shown in Figs. 8(a) and 8(b). To study the influence of asymmetry pair thickness d_2 on the Q-factor, it can be also described as two functions of d_2 plotted in Figs. 8(c) and 8(d), respectively.

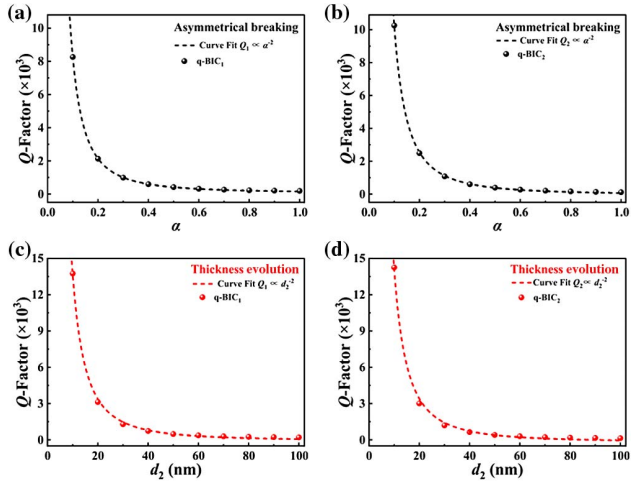

Fig. 8. Dependence of the Q-factor for the two q-BIC modes on the asymmetry parameter α and the asymmetry pair thickness d_2. (a), (c) q-BIC_1. (b), (d) q-BIC_2.

APPENDIX D: Q-FACTORS OF Si, MoS_2, AND STRONG COUPLING METASURFACES

We compare the Q-factors obtained from the Figs. 2(a) and 2(b), as shown in Table 2. With a fixed α of 0.9, we calculate the Q-factors of monolayer MoS_2 metasurface for varing d_3 in Table 3. For the strong coupling condition, the Q-factors of the 1L MoS_2 ($\theta = 10.40°$) re summarized in Table 4.

Table 2. Q-Factors of Si Metasurfaces for Varying α and d_2

α (d_1 = 100 nm)	0.9	0.7	0.5	0.3	0.1
Q_1	205	264	418	989	8262
Q_2	136	208	392	1081	10,258
d_2 [nm] (α = 0.9)	**90**	**70**	**50**	**30**	**10**
Q_1	227	293	481	1291	13,751
Q_2	152	221	404	1192	14,254

Table 3. Q-Factors of Monolayer MoS_2 Metasurface for Varying d_3

d_3 [nm] (α = 0.9)	50	30	10	0.65
Q_1	76	135	1280	1.0×10^6
Q_2	62	163	1870	1.4×10^6

Table 4. Q-Factors with a Strong Coupling for Different α

α	0.9	0.7	0.5	0.3	0.1
$Q \times 10^7$	0.56	0.74	1.25	2.92	22.50

Funding. National Safety Academy Foundation (U1830116, U2130112); National Natural Science Foundation of China (62175205); Youth Talent Support Program of Fujian Province (Eyas Plan of Fujian Province) ([2022]); Shenzhen Science and Technology Innovation Program (JCYJ20220530143015035); Agency for Science, Technology and Research (A20E5c0093, C210112019, C230917001, M21K2c0116, M22K2c0088, NRF2021-QEP2-03-P09).

Acknowledgment. We thank the National Model Microelectronics College at Xiamen University for providing equipment. In addition, Z.D. would like to acknowledge the funding support by Agency for Science, Technology and Research.

Disclosures. The authors declare no conflicts of interest.

Data Availability. Data underlying the results presented in this paper may be obtained from the authors upon reasonable request.

REFERENCES

1. M. Geissbuehler, L. Bonacina, V. Shcheslavskiy, *et al.*, "Nonlinear correlation spectroscopy (NLCS)," Nano Lett. **12**, 1668–1672 (2012).
2. J. Butet, I. Russier-Antoine, C. Jonin, *et al.*, "Sensing with multipolar second harmonic generation from spherical metallic nanoparticles," Nano Lett. **12**, 1697–701 (2012).

3. P. J. Campagnola and L. M. Loew, "Second-harmonic imaging microscopy for visualizing biomolecular arrays in cells, tissues and organisms," Nat. Biotechnol. **21**, 1356–1360 (2003).
4. J. Yao, R. Lin, M. K. Chen, *et al.*, "Integrated-resonant metadevices: a review," Adv. Photon. **5**, 024001 (2023).
5. X. Zhang, L. He, X. Gan, *et al.*, "Quasi-bound states in the continuum enhanced second-harmonic generation in thin-film lithium niobate," Laser Photon. Rev. **16**, 2200031 (2022).
6. F. J. F. Löchner, A. N. Fedotova, S. Liu, *et al.*, "Polarization-dependent second harmonic diffraction from resonant GaAs metasurfaces," ACS Photon. **5**, 1786–1793 (2018).
7. P. P. Vabishchevich, S. Liu, M. B. Sinclair, *et al.*, "Enhanced second-harmonic generation using broken symmetry III–V semiconductor fano metasurfaces," ACS Photon. **5**, 1685–1690 (2018).
8. Z. Dai, G. Hu, Q. Ou, *et al.*, "Artificial metaphotonics born naturally in two dimensions," Chem. Rev. **120**, 6197–6246 (2020).
9. J. You, Y. Luo, J. Yang, *et al.*, "Hybrid/integrated silicon photonics based on 2D materials in optical communication nanosystems," Laser Photon. Rev. **14**, 2000239 (2020).
10. H. Lin, Z. Zhang, H. Zhang, *et al.*, "Engineering van der Waals materials for advanced metaphotonics," Chem. Rev. **122**, 15204–15355 (2022).
11. J. Shi, X. Wu, K. Wu, *et al.*, "Giant enhancement and directional second harmonic emission from monolayer WS_2 on silicon substrate via Fabry-Pérot micro-cavity," ACS Nano **16**, 13933–13941 (2022).
12. Z. Wang, Z. Dong, H. Zhu, *et al.*, "Selectively plasmon-enhanced second-harmonic generation from monolayer tungsten diselenide on flexible substrates," ACS Nano **12**, 1859–1867 (2018).
13. J. Yao, J.-Y. Ou, V. Savinov, *et al.*, "Plasmonic anapole metamaterial for refractive index sensing," PhotoniX **3**, 23 (2022).
14. S. Busschaert, R. Reimann, M. Cavigelli, *et al.*, "Transition metal dichalcogenide resonators for second harmonic signal enhancement," ACS Photon. **7**, 2482–2488 (2020).
15. S. I. Azzam and A. V. Kildishev, "Photonic bound states in the continuum: from basics to applications," Adv. Opt. Mater. **9**, 2001469 (2020).
16. D. Lin, P. Fan, E. Hasman, *et al.*, "Dielectric gradient metasurface optical elements," Science **345**, 298–302 (2014).
17. Y. Liang, H. Lin, S. Lin, *et al.*, "Hybrid anisotropic plasmonic metasurfaces with multiple resonances of focused light beams," Nano Lett. **21**, 8917–8923 (2021).
18. I. S. Sinev, K. Koshelev, Z. Liu, *et al.*, "Observation of ultrafast self-action effects in quasi-BIC resonant metasurfaces," Nano Lett. **21**, 8848–8855 (2021).
19. K. Koshelev, A. Bogdanov, and Y. Kivshar, "Meta-optics and bound states in the continuum," Sci. Bull. **64**, 836–842 (2019).
20. G. Zograf, K. Koshelev, A. Zalogina, *et al.*, "High-harmonic generation from resonant dielectric metasurfaces empowered by bound states in the continuum," ACS Photon. **9**, 567–574 (2022).
21. Z. Dong, L. Jin, S. D. Rezaei, *et al.*, "Schrödinger's red pixel by quasi-bound-states-in-the-continuum," Sci. Adv. **8**, eabm4512 (2022).
22. Z. Dong, Z. Mahfoud, R. Paniagua-Domínguez, *et al.*, "Nanoscale mapping of optically inaccessible bound-states-in-the-continuum," Light Sci. Appl. **11**, 20 (2022).
23. N. Bernhardt, K. Koshelev, S. J. U. White, *et al.*, "Quasi-BIC resonant enhancement of second-harmonic generation in WS_2 monolayers," Nano Lett. **20**, 5309–5314 (2020).
24. L. Kuhner, L. Sortino, B. Tilmann, *et al.*, "High-*Q* nanophotonics over the full visible spectrum enabled by hexagonal boron nitride metasurfaces," Adv. Mater. **35**, e2209688 (2023).
25. L. Kuhner, L. Sortino, R. Berte, *et al.*, "Radial bound states in the continuum for polarization-invariant nanophotonics," Nat. Commun. **13**, 4992 (2022).
26. T. C. Tan, Y. K. Srivastava, R. T. Ako, *et al.*, "Active control of nanodielectric-induced THz quasi-BIC in flexible metasurfaces: a platform for modulation and sensing," Adv. Mater. **33**, e2100836 (2021).
27. M. V. Rybin, K. L. Koshelev, Z. F. Sadrieva, *et al.*, "High-*Q* supercavity modes in subwavelength dielectric resonators," Phys. Rev. Lett. **119**, 243901 (2017).
28. Q. Hong, X. Chen, J. Zhang, *et al.*, "Remarkably high-*Q* resonant nanostructures based on atomically thin two-dimensional materials," Nanoscale **11**, 23149–23155 (2019).
29. L. Huang, R. Jin, C. Zhou, *et al.*, "Ultrahigh-*Q* guided mode resonances in an all-dielectric metasurface," Nat. Commun. **14**, 3433 (2023).
30. Y. An, Y. Tian, C. Wei, *et al.*, "Recent advances and perspectives of 2D silicon: synthesis and application for energy storage and conversion," Energy Storage Mater. **32**, 115–150 (2020).
31. W. T. Hsu, Z. A. Zhao, L. J. Li, *et al.*, "Second harmonic generation from artificially stacked transition metal dichalcogenide twisted bilayers," ACS Nano **8**, 2951–2958 (2014).
32. E. D. Palik, *Handbook of Optical Constants of Solids* (Academic, 1997).
33. M. Nauman, J. Yan, D. de Ceglia, *et al.*, "Tunable unidirectional nonlinear emission from transition-metal-dichalcogenide metasurfaces," Nat. Commun. **12**, 5597 (2021).
34. D. I. Yakubovsky, Y. V. Stebunov, R. V. Kirtaev, *et al.*, "Ultrathin and ultrasmooth gold films on monolayer MoS_2," Adv. Mater. Interfaces **6**, 1900196 (2019).
35. G. A. Ermolaev, Y. V. Stebunov, A. A. Vyshnevyy, *et al.*, "Broadband optical properties of monolayer and bulk MoS_2," npj 2D Mater. Appl. **4**, 21 (2020).
36. R. W. Boyd, *Nonlinear Optics*, 3rd ed. (Springer, 2008).
37. L. Qu, L. Bai, C. Jin, *et al.*, "Giant second harmonic generation from membrane metasurfaces," Nano Lett. **22**, 9652–9657 (2022).
38. C. W. Hsu, B. Zhen, A. D. Stone, *et al.*, "Bound states in the continuum," Nat. Rev. Mater. **1**, 16048 (2016).
39. A. Aigner, A. Tittl, J. Wang, *et al.*, "Plasmonic bound states in the continuum to tailor light-matter coupling," Sci. Adv. **8**, eadd4816 (2022).
40. K. Koshelev, Y. Tang, K. Li, *et al.*, "Nonlinear metasurfaces governed by bound states in the continuum," ACS Photon. **6**, 1639–1644 (2019).
41. J. Wang, J. Kühne, T. Karamanos, *et al.*, "All-dielectric crescent metasurface sensor driven by bound states in the continuum," Adv. Funct. Mater. **31**, 2104652 (2021).
42. S. Han, M. V. Rybin, P. Pitchappa, *et al.*, "Guided-mode resonances in all-dielectric terahertz metasurfaces," Adv. Opt. Mater. **8**, 1900959 (2019).
43. G. Quaranta, G. Basset, O. J. F. Martin, *et al.*, "Recent advances in resonant waveguide gratings," Laser Photon. Rev. **12**, 1800017 (2018).
44. Y. Chen, C. Zhao, Y. Zhang, *et al.*, "Integrated molar chiral sensing based on high-*Q* metasurface," Nano Lett. **20**, 8696–8703 (2020).
45. X. Liu, T. Galfsky, Z. Sun, *et al.*, "Strong light–matter coupling in two-dimensional atomic crystals," Nat. Photonics **9**, 30–34 (2014).
46. L. Zhang, R. Gogna, W. Burg, *et al.*, "Photonic-crystal exciton-polaritons in monolayer semiconductors," Nat. Commun. **9**, 713 (2018).
47. T. Weber, L. Kuhner, L. Sortino, *et al.*, "Intrinsic strong light-matter coupling with self-hybridized bound states in the continuum in van der Waals metasurfaces," Nat. Mater. **22**, 970–976 (2023).
48. S. Joseph, S. Sarkar, S. Khan, *et al.*, "Exploring the optical bound state in the continuum in a dielectric grating coupled plasmonic hybrid system," Adv. Opt. Mater. **9**, 2001895 (2021).
49. T. Santiago-Cruz, S. D. Gennaro, O. Mitrofanov, *et al.*, "Resonant metasurfaces for generating complex quantum states," Science **377**, 991–995 (2022).
50. J. Yao, Y. Yin, L. Ye, *et al.*, "Enhancing third-harmonic generation by mirror-induced electric quadrupole resonance in a metal-dielectric nanostructure," Opt. Lett. **45**, 5864–5867 (2020).
51. L. Carletti, A. Zilli, F. Moia, *et al.*, "Steering and encoding the polarization of the second harmonic in the visible with a monolithic $LiNbO_3$ metasurface," ACS Photon. **8**, 731–737 (2021).
52. J. Ma, F. Xie, W. Chen, *et al.*, "Nonlinear lithium niobate metasurfaces for second harmonic generation," Laser Photon. Rev. **15**, 2000521 (2021).
53. F. J. F. Löchner, A. George, K. Koshelev, *et al.*, "Hybrid dielectric metasurfaces for enhancing second-harmonic generation in chemical vapor deposition grown MoS_2 monolayers," ACS Photonics **8**, 218–227 (2020).
54. R. Biswas, A. Prosad, L. A. S. Krishna, *et al.*, "Evolutionary design of two-dimensional material Fabry-Perot structures for enhanced second harmonic generation," Nanophotonics **12**, 29–42 (2023).
55. H. M. Gramling, C. M. Towle, S. B. Desai, *et al.*, "Spatially precise transfer of patterned monolayer WS_2 and MoS_2 with features larger than 104 μm^2 directly from multilayer sources," ACS Appl. Electron. Mater. **1**, 407–416 (2019).